THE STRUCTURE OF THE BROAD-LINE REGION IN ACTIVE GALACTIC NUCLEI.
I. RECONSTRUCTED VELOCITY-DELAY MAPS

C. J. GRIER[1], B. M. PETERSON[1,2], KEITH HORNE[3], M. C. BENTZ[4], R. W. POGGE[1,2], K. D. DENNEY[5], G. DE ROSA[1],
PAUL MARTINI[1,2], C. S. KOCHANEK[1,2], Y. ZU[1], B. SHAPPEE[1], R. SIVERD[6], T. G. BEATTY[1], S. G. SERGEEV[7], S. KASPI[8,9],
C. ARAYA SALVO[1], J. C. BIRD[1], D. J. BORD[10], G. A. BORMAN[7,11], X. CHE[12], C. CHEN[13], S. A. COHEN[13], M. DIETRICH[1],
V. T. DOROSHENKO[7,14], YU. S. EFIMOV[7,17], N. FREE[15], I. GINSBURG[13], C. B. HENDERSON[1], A. L. KING[12], K. MOGREN[1],
M. MOLINA[1,16], A. M. MOSQUERA[1], S. V. NAZAROV[7,11], D. N. OKHMAT[7,11], O. PEJCHA[1], S. RAFTER[9], J. C. SHIELDS[15],
J. SKOWRON[1], D. M. SZCZYGIEL[1], M. VALLURI[12], AND J. L. VAN SADERS[1]
[1] Department of Astronomy, The Ohio State University, 140 W 18th Ave, Columbus, OH 43210, USA
[2] Center for Cosmology & AstroParticle Physics, The Ohio State University, 191 West Woodruff Ave, Columbus, OH 4321, USA
[3] SUPA Physics & Astronomy, University of St. Andrews, Fife, KY16 9SS Scotland, UK
[4] Department of Physics and Astronomy, Georgia State University, Astronomy Offices, One Park Place South SE, Suite 700, Atlanta, GA 30303, USA
[5] Marie Curie Fellow at the Dark Cosmology Centre, Niels Bohr Institute, University of Copenhagen, Juliane Maries Vej 30, DK-2100 Copenhagen, Denmark
[6] Department of Physics and Astronomy, Vanderbilt University, 5301 Stevenson Center, Nashville, TN 37235, USA
[7] Crimean Astrophysical Observatory, P/O Nauchny Crimea 98409, Ukraine
[8] School of Physics and Astronomy, Raymond and Beverly Sackler Faculty of Exact Sciences, Tel Aviv University, Tel Aviv 69978, Israel
[9] Physics Department, Technion, Haifa 32000, Israel
[10] Department of Natural Sciences, The University of Michigan - Dearborn, 4901 Evergreen Rd, Dearborn, MI 48128, USA
[11] Isaac Newton Institute of Chile, Crimean Branch, Ukraine
[12] Department of Astronomy, University of Michigan, 500 Church Street, Ann Arbor, MI 41809, USA
[13] Department of Physics and Astronomy, Dartmouth College, 6127 Wilder Laboratory, Hanover, NH 03755, USA
[14] South Station of the Moscow MV Lomonosov State University, Moscow, Russia, P/O Nauchny, 98409 Crimea, Ukraine
[15] Department of Physics & Astronomy, Ohio University, Athens, OH 45701, USA
[16] Department of Astronomy & Astrophysics, The Pennsylvania State University, 525 Davey Lab, University Park, PA 16802, USA

ABSTRACT

We present velocity-resolved reverberation results for five active galactic nuclei. We recovered velocity-delay maps using the maximum entropy method for four objects: Mrk 335, Mrk 1501, 3C 120, and PG 2130+099. For the fifth, Mrk 6, we were only able to measure mean time delays in different velocity bins of the Hβ emission line. The four velocity-delay maps show unique dynamical signatures for each object. For 3C 120, the Balmer lines show kinematic signatures consistent with both an inclined disk and infalling gas, but the He II λ4686 emission line is suggestive only of inflow. The Balmer lines in Mrk 335, Mrk 1501, and PG 2130+099 show signs of infalling gas, but the He II emission in Mrk 335 is consistent with an inclined disk. We also see tentative evidence of combined virial motion and infalling gas from the velocity-binned analysis of Mrk 6. The maps for 3C 120 and Mrk 335 are two of the most clearly defined velocity-delay maps to date. These maps constitute a large increase in the number of objects for which we have resolved velocity-delay maps and provide evidence supporting the reliability of reverberation-based black hole mass measurements.

Key words: galaxies: active – galaxies: nuclei – galaxies: Seyfert

Online-only material: color figure

1. INTRODUCTION

One of the continuing mysteries in the studies of active galactic nuclei (AGNs) is the structure and kinematics of the broad-line region (BLR). It is generally accepted that AGNs are powered by supermassive black holes, and the broad emission lines seen in Type 1 AGNs are the result of the photoionization of gas in the BLR. Under the assumption that this gas is in virial motion around the black hole, we can use it to measure the mass of the black hole itself. However, it is impossible to study the structure of the BLR directly because the BLR is on the order of light-days in radius, which renders it spatially unresolvable even in the nearest of galaxies with the largest diffraction-limited telescopes. The unknown BLR structure introduces uncertainties in any black hole mass measurements derived from BLR gas kinematics. To learn about the BLR structure, we must rely on either reverberation mapping techniques (e.g., Peterson et al. 2004) or microlensing of gravitationally lensed quasars (e.g., Guerras et al. 2012). Reverberation techniques use the

time variability observed in the AGN continuum emission and the subsequent response of the gas in the BLR (Blandford & McKee 1982; Peterson 1993). By monitoring the AGN spectra over a period of time, we can determine the distance of the emitting gas from the central source by measuring the time delay between variations in the continuum and the response of the emission lines. This time delay is due to the light-travel time between the continuum source and the BLR.

The variations in the BLR emission-line flux, $\Delta L(V, t)$, are a convolution of the continuum flux variations, $\Delta C(t)$, with the "transfer function," $\Psi(V, \tau)$ (Blandford & McKee 1982). The transfer function depends on the temporal lag τ between the line and continuum emission, and the line-of-sight velocity V of the BLR gas. The relationship is expressed mathematically as

$$\Delta L(V, t) = \int_0^\infty \Psi(V, \tau)\Delta C(t - \tau)d\tau. \qquad (1)$$

A main goal of reverberation mapping is to recover $\Psi(V, \tau)$, called the "velocity-delay map," which describes how the

---

[17] Deceased, 2011 October 21.

continuum flux variations give rise to BLR flux variations, and therefore contains information about the BLR geometry and kinematics. For example, a Keplerian disk produces a velocity-symmetric structure with a wider/narrower range of velocities at smaller/larger delays. In contrast, radial flows give rise to asymmetric velocity structure, the signature of infall/outflow being smaller delays on the red/blue side of the velocity profile. Most previous reverberation studies have been limited to measuring the mean time delay $\langle\tau\rangle$ for various emission lines. This allows us to estimate the mean radius of the BLR (e.g., Peterson et al. 2004; Denney et al. 2010; Bentz et al. 2010b; Grier et al. 2012), but it reveals very little information about the detailed structure of the BLR.

It has long been recognized that measuring emission-line time lags as a function of line-of-sight velocity provides a way to determine the gross kinematics of the BLR (e.g., Bahcall et al. 1972; Blandford & McKee 1982; Bochkarev & Antokhin 1982; Capriotti et al. 1982; Antokhin & Bochkarev 1983), although it is only relatively recently that suitable data have become available to achieve this in practice. There were a number of early attempts to extract velocity-dependent time lags in emission lines in order to probe the BLR kinematics, though these were generally frustrated by low data quality, time-sampling issues, or both. The first attempts that we are aware of to search for velocity-dependent lags were by Gaskell (1988) for NGC 4151 and Koratkar & Gaskell (1989) for Fairall 9, in both cases for the C IV $\lambda1549$ emission line based on data obtained with the *International Ultraviolet Explorer* (*IUE*; a mean lag for Fairall 9 had been obtained earlier by Clavel et al. 1989). In both cases, detection of infall was claimed. We have, however, reanalyzed both of these data sets using more modern methods and find that the light curves are far too poorly sampled to support either claim of a detection of infall. Later, Clavel et al. (1990) revisited the case of NGC 4151 with improved time sampling. To within the accuracy of their measurement, they found the red and blue wings of C IV to vary simultaneously. However, their mean sampling interval of 3.4 days was only slightly smaller than the C IV mean response time, which would have made it difficult to detect the subtle velocity-dependent lags that have been detected in optical lines in recent years (Denney et al. 2009; Bentz et al. 2010b).

The first well-sampled AGN emission-line light curves became available as a result of intensive monitoring of NGC 5548 with *IUE* (Clavel et al. 1991) and ground-based telescopes (Peterson et al. 1991; Dietrich et al. 1993) in 1988–89. These data led to the first successful attempts to recover one-dimensional delay maps, $\Psi(\tau)$ (Horne et al. 1991; Krolik et al. 1991). Other attempts were also made to search for velocity-dependent lags (e.g., Clavel 1991, for NGC 5548), but they generally concluded that any velocity-dependent lags remained unresolved. However, Crenshaw & Blackwell (1990) argued that C IV profile variations during part of the 1988–89 campaign on NGC 5548 indicated infall of BLR gas, although an infall signature was not detected using any other subset of the campaign data and the *IUE* spectra were generally rather marginal for AGN emission-line profile studies. Other sources were searched for velocity-dependent emission-line responses, but these searches were also unsuccessful (e.g., Kollatschny & Dietrich 1997). Some limited success was achieved with both space-based observations (Ulrich & Horne 1996; Wanders et al. 1995) and ground-based data (Kollatschny 2003), but except in the case of NGC 4151 (Ulrich & Horne 1996) the resulting velocity-delay maps showed little clear structure. There was

Table 1
Object List

Object	R.A. (J2000)	Decl. (J2000)	z
Mrk 335	00 06 19.5	+20 12 10	0.0258
Mrk 1501	00 10 31.0	+10 58 30	0.0893
3C 120	04 33 11.1	+05 21 16	0.0330
Mrk 6	06 52 12.2	+74 25 37	0.0188
PG 2130+099	21 32 27.8	+10 08 19	0.0630

also a growing understanding that the dramatic emission-line profile variations observed in some sources were not a reverberation effect (e.g., Wanders & Peterson 1996; Sergeev et al. 2007), and that reverberation signals were generally going to be weak. Obtaining a high-fidelity velocity–delay map was going to require both high-quality data and excellent temporal sampling (Horne et al. 2004). More recent spectroscopic monitoring campaigns for reverberation-mapping have been specifically designed to, among other things, recover velocity-delay maps (e.g., Bentz et al. 2010b, Denney et al. 2011). These efforts have already been shown to be successful—Bentz et al. (2010a) show well-resolved velocity-delay maps for Arp 151 using maximum entropy methods, and Pancoast et al. (2012) used dynamical modeling (first described by Pancoast et al. 2011) to recover BLR structure information in Mrk 50.

In late 2010, we carried out a four-month long reverberation mapping campaign with the ultimate goal of recovering velocity-delay maps for several of the targets. Details of the data processing, light curves, mean time lags, and black hole mass measurements for these objects were published by Grier et al. (2012). Here we present velocity-binned reverberation results for all five objects observed in our 2010 campaign and two-dimensional velocity-delay maps for four objects. All five targets and their coordinates and redshifts are listed in Table 1. While our reverberation campaign was aimed primarily at investigating the Hβ emission line, in a few cases we recover velocity-delay maps for the Hγ and He II $\lambda4686$ emission lines as well.

2. DATA

For this study we use spectroscopic and photometric data obtained during our reverberation campaign carried out at multiple institutions in late 2010. The primary set of spectra were obtained using the Boller and Chivens CCD spectrograph on the MDM 1.3 m McGraw-Hill telescope on Kitt Peak. We supplemented our spectroscopic continuum light curves with photometry from the 46 cm Centurion telescope at Wise Observatory of Tel-Aviv University and the 70 cm telescope at the Crimean Astrophysical Observatory (CrAO), and with spectra obtained from the 2.6 m Shajn telescope at CrAO. All data were obtained between 2010 August 21 and 2011 January 7. The data processing is described in detail in Grier et al. (2012). In short, we calibrated the reduced spectra onto an absolute flux scale by assuming that the flux in the narrow [O III] $\lambda5007$ emission line is constant. We created a reference spectrum for each object using the spectra taken on photometric nights during the campaign. We then used the procedure of van Groningen & Wanders (1992) to apply small wavelength shifts and scale each individual spectrum to match the flux in the [O III] $\lambda5007$ emission line in the reference spectrum using a χ^2 goodness-of fit estimator method. The resulting scaled spectra were used to create the driving continuum light curves used throughout our
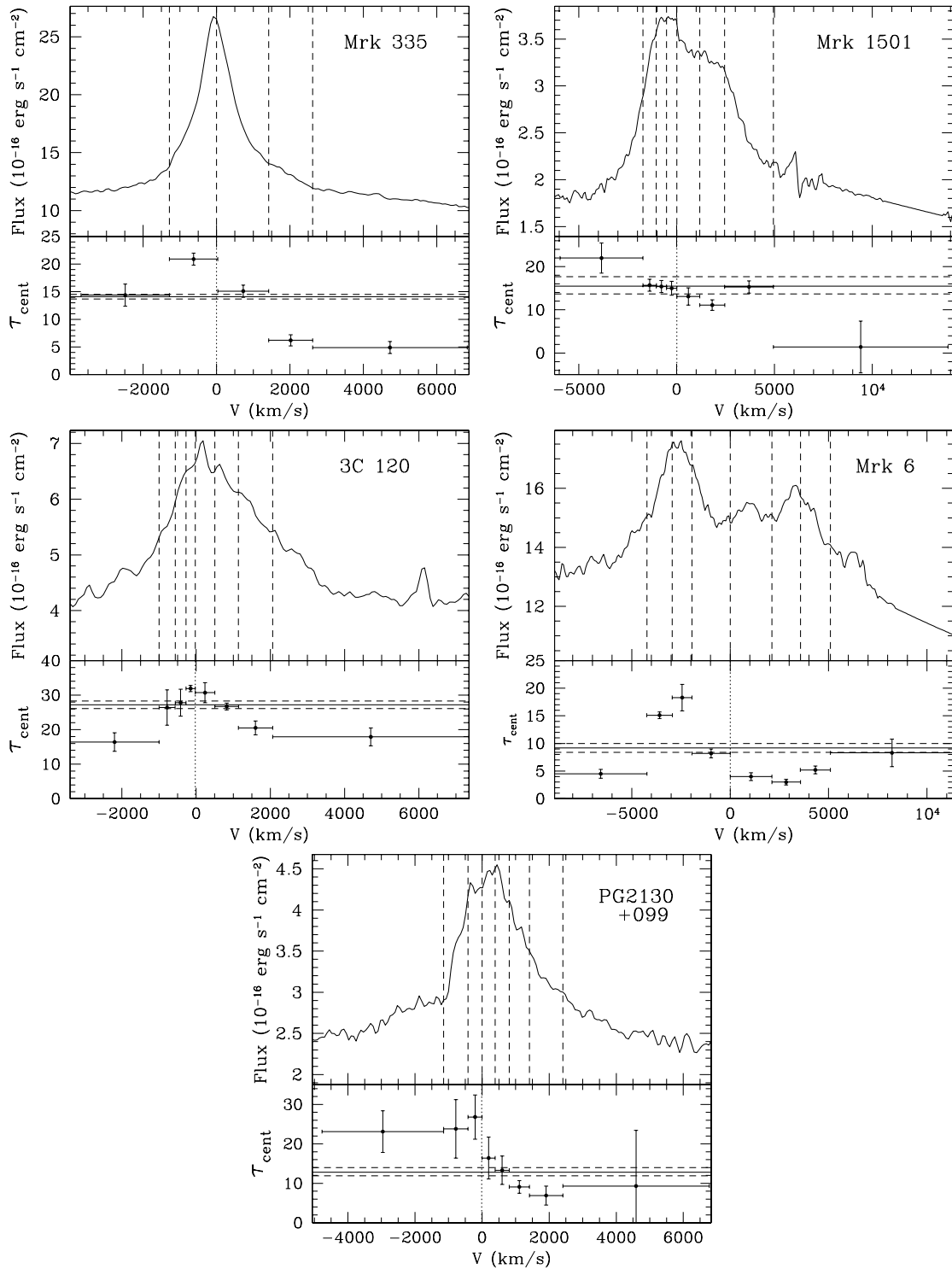
Figure 1. Velocity-binned reverberation lag results. The top panels show the rms residual spectrum for each object, with the edges of the bins designated by vertical dashed lines. The bottom panels show the mean time delays measured for each bin. The zero-velocity center of the Hβ emission line is shown by the dotted line. The horizontal solid line shows the average time lag reported in Grier et al. (2012), with uncertainties as horizontal dashed lines. Error bars in the velocity direction show the width of the bins.

analysis as well as the light curves used in our velocity-binned time series analysis.

3. INITIAL Hβ VELOCITY-BINNED TIME SERIES ANALYSIS

As a preliminary step, we first searched for gross kinematic signatures by seeing whether different parts of each emission line show different time delays with respect to the continuum. Following Denney et al. (2009), we divided the Hβ emission line into velocity bins as follows. First, we divide the Hβ emission lines in half at the zero-velocity line center (the systemic redshift), to separate redshifted and blueshifted signals. We then divide each line half into bins containing equal flux in the rms residual spectrum, choosing the number of bins for each object based on the width of the rms line profiles. We create light curves
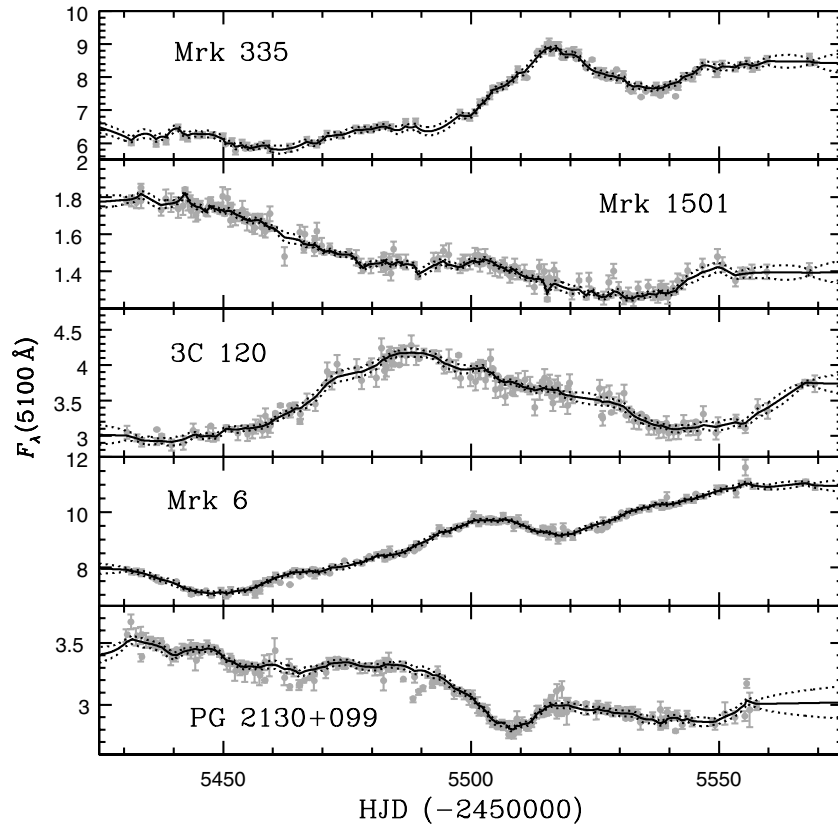
Figure 2. Original continuum light curves (gray data points) from Grier et al. (2012) and the JAVELIN mean continuum model (black solid line) used in the MEMECHO analysis. The dotted line shows the standard deviation about the mean light curve from individual model realizations. Fluxes are given in units of 10^{-15} erg s^{-1} cm^{-2} Å^{-1}.

for individual bins by integrating the flux within each bin in each scaled spectrum. The resulting light curves were analyzed using JAVELIN, the updated version of SPEAR (see Zu et al. 2011 and Grier et al. 2012 for details), to measure the time delay in each light curve with respect to the continuum light curve. In essence, JAVELIN uses a statistical model of the continuum light curve and its covariances and simultaneously fits the continuum and line light curves assuming a simple top-hat transfer function. This leads to a statistically well-defined means of interpolating the irregularly sampled line and continuum data that essentially averages over all possible interpolated light curves weighted by their likelihood of fitting the data. In particular, the model fills gaps in the light curves in a well-defined manner with well-defined uncertainties.

Our results from JAVELIN are shown in Figure 1. The top panels show the rms residual line profile and the wavelength bins, and the bottom panel shows the distribution of lags for each part of the emission line. As a check, we also ran the light curves for each bin through a cross correlation analysis routine that is widely used in reverberation mapping (e.g., Peterson et al. 2004). The lags from the cross correlation were nearly identical to the ones obtained from JAVELIN. We show here only the JAVELIN results, since the JAVELIN uncertainties are much smaller than those obtained through cross correlation methods and the overall signatures are the same. In all five objects, we see velocity-dependent time lags in the Hβ emission line. Mrk 335, Mrk 1501, and PG 2130+099 all show longer time lags on the blue side of the line profile than on the red side, which is a signature of inflowing gas. By contrast, 3C 120 shows a nearly symmetric profile, with small lags in the outer wings, and larger lags toward the line center, which is suggestive of a disk. Mrk 6

shows more complex structures that could be a combination of a disk plus infall, as previously suggested by Doroshenko et al. (2012) for this object.

4. TWO-DIMENSIONAL MEMECHO FITTING

4.1. Preparation of Spectra

To recover the velocity-delay maps, we used maximum entropy methods as implemented in the program MEMECHO (see Horne et al. 1991 and Horne 1994 for details). To prepare the data for use with MEMECHO, we used software developed by Keith Horne called PREPSPEC. PREPSPEC applies corrections to account for wavelength shifts due to instrument flexure and differential refraction, spectral blurring due to seeing and instrumental resolution, and errors due to slit losses and changes in atmospheric transmission between epochs. To do this, we fit a calibration model to the spectra that accounts for both the spectral variability and the above-mentioned systematic errors. We model the spectra as the sum of five different components: (1) a constant "mean" spectrum, which accounts for non-varying components of the continuum and broad emission lines as well as starlight from the host galaxy, (2) non-varying narrow emission lines, (3) a time-variable continuum, (4) time variable broad emission lines, and (5) factors to account for wavelength shift, spectral blurring, and scaling. After subtracting the models from the spectra, the resulting continuum-subtracted line profile variations are used as inputs to MEMECHO.

4.2. MEM Fitting

In brief, MEMECHO finds the "simplest" linearized echo model that fits the observed continuum and emission-line
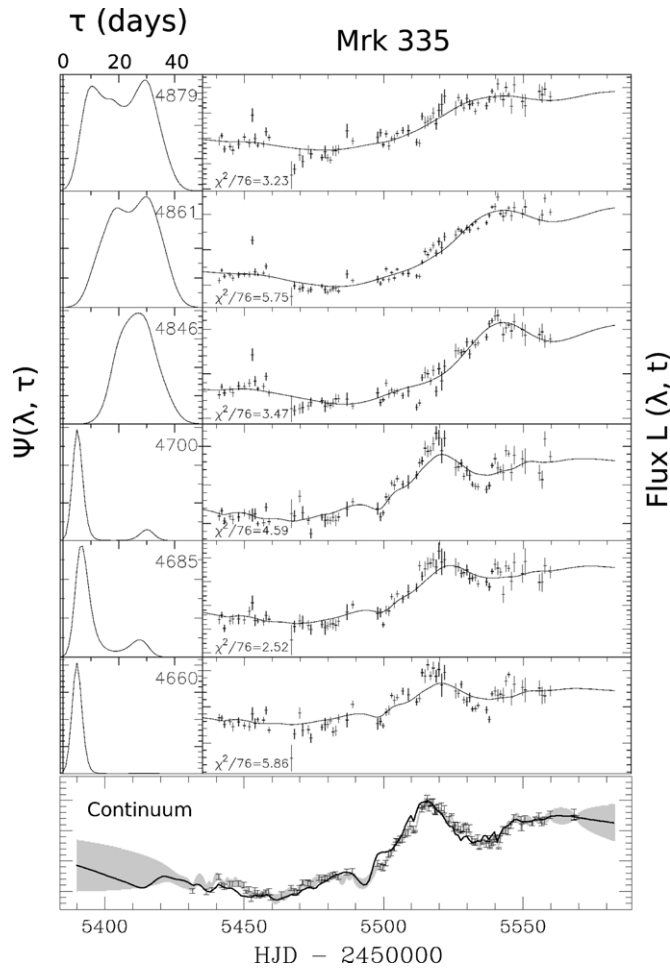
4

Figure 3. Best MEMECHO fits to the spectra of Mrk 335. The left panels show the delay maps at each selected rest-frame wavelength, given in the top right-hand corner of each panel. The right panels show the emission-line light curve at these selected wavelengths and the MEMECHO fit to the light curve. The χ^2/N of the fit for each light curve is shown in each panel. The bottom panel shows the original continuum light curve (black error bars), the error envelope from the simulated light curve showing the standard deviation about the mean (gray envelope), and the continuum model from MEMECHO (solid black line).

Figure 4. Best MEMECHO fits to the spectra of Mrk 1501. Panels and symbols are the same as in Figure 3.

spectral variations. This is accomplished by minimizing the function

$$Q = \chi^2 - 2\,\alpha\,S \qquad (2)$$

for a given model fit to a set of data. Here χ^2 measures the "badness-of-fit" between N data points with values D_k and the corresponding model predictions μ_k for those values, assuming Gaussian errors with known variances σ_k^2. The entropy S measures the "simplicity" of the model, elaborated below, and the regularization parameter α controls the trade-off between these competing requirements. MEMECHO adjusts α and the model parameters p_i to achieve a user-specified value of χ^2/N while maximizing S.

In MEMECHO's linearized echo model

$$L(\lambda, t) = L_0(\lambda) + \int_0^\infty \Psi(\lambda, \tau)(C(t - \tau) - C_0)d\tau, \qquad (3)$$

the parameters p_i include the continuum light curve $C(t)$ on an evenly spaced grid, the delay map at each wavelength $\Psi(\lambda, \tau)$, and the time-independent background spectrum $L_0(\lambda)$. C_0 is a reference continuum level, which we set at the median of the
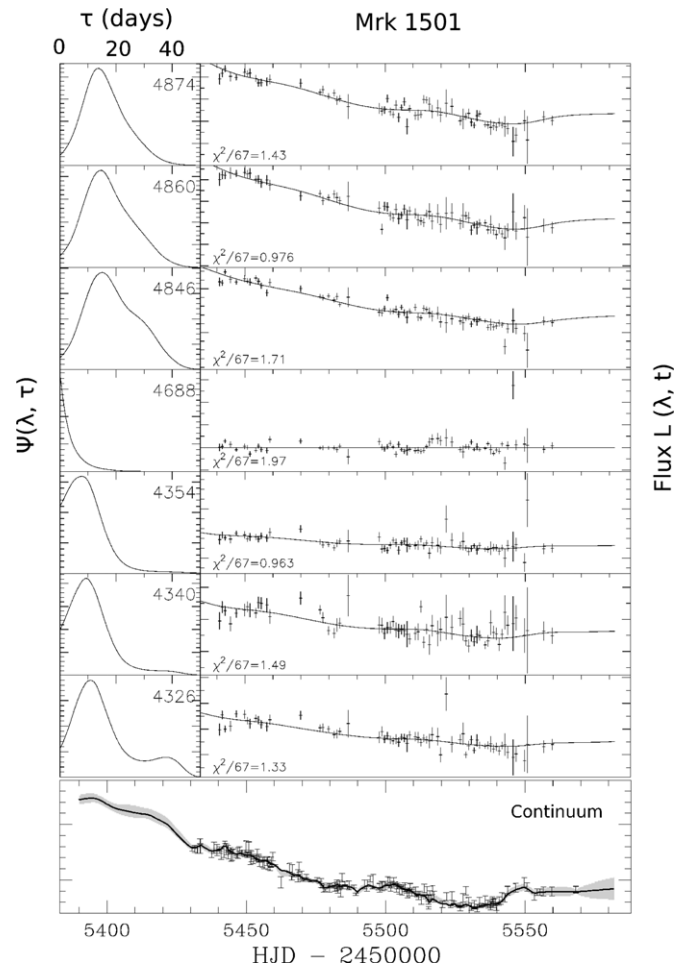
continuum light curve data. The entropy of the model is defined as

$$S = \sum_i w_i(p_i - q_i - p_i \ln(p_i/q_i)), \qquad (4)$$

where w_i are weights, p_i are the positive parameters outlined above, and q_i are the default values of these parameters. Note that S is maximized when $p_i = q_i$. Minimizing Q gives

$$0 = \sum_{k=1}^N \frac{D_k - \mu_k}{\sigma_k^2} \frac{d\mu_k}{dp_i} + \alpha\,w_i\,\ln(p_i/q_i). \qquad (5)$$

Thus the model parameters p_i are pulled by the data toward $\mu_k = D_k$ and by the entropy toward $p_i = q_i$, with α adjusting the trade-off between the two. With default values $q_i = (p_{i-1}\,p_{i+1})^{1/2}$, the entropy "pulls" each p_i toward the geometric mean of its neighbors, so that the entropy penalizes regions of high curvature and favors smooth functions with Gaussian features and exponential tails. The weights w_i and default values q_i are assigned with two parameters in MEMECHO: W to stiffen $\Psi(\lambda, \tau)$ relative to $C(t)$, and A to control the aspect ratio of features in $\Psi(\lambda, \tau)$. The A and W parameters are set by the user. Their qualitative effects on the velocity-delay maps are described below in Section 5.2.1.

4.3. The Driving Continuum Light Curve

One of the major practical issues with the use of MEMECHO is its tendency to introduce spurious features at gaps in the
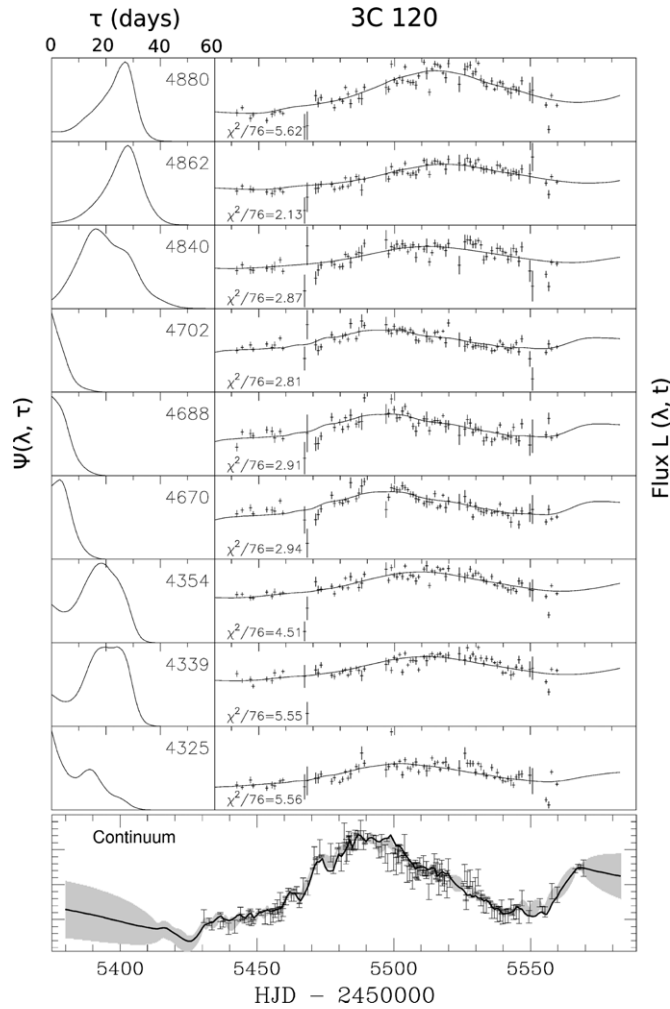
Figure 5. Best MEMECHO fits to the spectra of 3C 120. Panels and symbols are the same as in Figure 3.

Figure 6. Best MEMECHO fits to the spectra of Mrk 6. Panels and symbols are the same as in Figure 3.

continuum light curve to drive χ^2/N to the minimum value set by the user. This becomes a significant problem as the target χ^2/N decreases. Altering MEMECHO parameters to stiffen (i.e., penalize rapid variations in) the driving light curve is sometimes helpful, but we were still unable to produce velocity-delay maps with any discernible structure using the original continuum light curves. To provide stronger constraints on the driving light curve model, we ran our full continuum light curves (including both spectroscopic and photometric data) through the JAVELIN modeling software of Zu et al. (2011). This method models the continuum with a damped random walk (DRW) model that has been demonstrated to be a good statistical model of AGN variability (e.g., Kelly et al. 2009; Kozłowski et al. 2010; MacLeod et al. 2010; MacLeod et al. 2012; Zu et al. 2012). This allowed us to create highly sampled *simulated* continuum light curves with reliable uncertainties that represent the range of the most likely continuum behavior within the gaps. Instead of providing MEMECHO with our original continuum light curve, we use our highly sampled JAVELIN mean light curve, which more strongly constrains the MEMECHO continuum model. This light curve is the probability-weighted mean of DRW light curves consistent with the data and the DRW model. Uncertainties on each point in the simulated light curve represent the standard deviation of probable light curves around this mean. These narrow to match the measurement errors of the data points
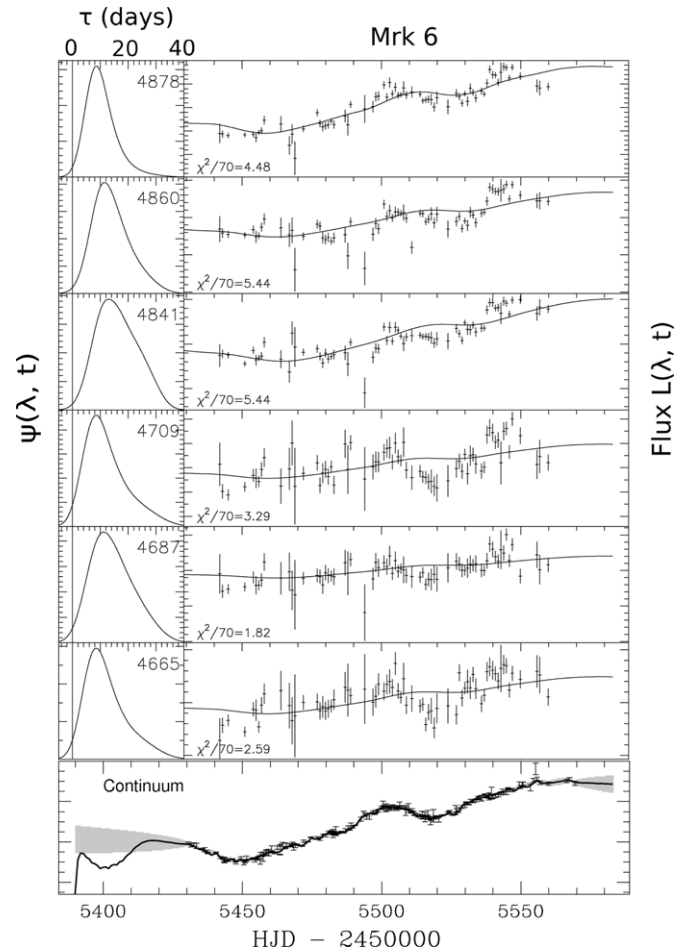
and then broaden as the gaps between the data become larger. The variability observed in the adopted mean simulated light curve is somewhat smoothed compared with an individual DRW model realization, but the error envelope applied to the mean light curve, representing the 1σ deviations of the individual realizations about the mean, accounts for these differences. The original continuum light curves and their corresponding simulated light curves are shown in Figure 2.

Using the JAVELIN mean continuum light curve allows us to fit the variability of both the continuum and the rest of the spectrum to much higher degrees of accuracy and keep MEMECHO from introducing spurious features into our light curves and by extension, into the derived echo maps. Light curves, one-dimensional MEMECHO fits, and recovered delay maps at selected wavelengths are shown in Figures 3–7 for all five objects. The wavelengths for the fits and delay maps shown in these figures were chosen to show the response in the red and blue wings as well as at the center of each emission line. One thing to note is that using the probability-weighted mean as the constraint on the MEMECHO construction of the continuum means that we are over-smoothing the light curves because we are neglecting the covariance of light curve deviations from the mean, which may weaken short-timescale variability. This will also cause some difficulty in the fitting, as it can force the light curve models to be smoother than the data. At the same time, the χ^2/N value reported by MEMECHO is no longer strictly valid—the deviations of any particular light curve model from
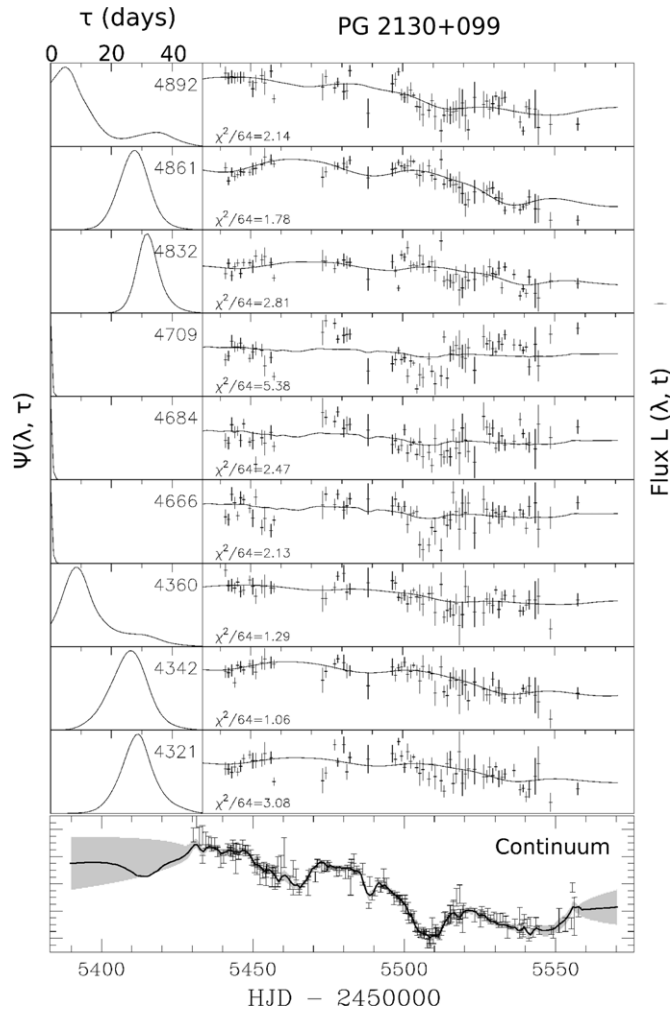
Figure 7. Best MEMECHO fits to the spectra of PG 2130+099. Panels and symbols are the same as in Figure 3.

Table 2
MEMECHO Parameters[a]

Object	A	W	τ_{min}	χ^2/N
Mrk 335	0.1	1.0	-1	2.8
Mrk 1501	1.0	1.0	0	1.8
3C 120	1.0	1.0	0	2.4
PG 2130+099	0.1	1.0	0	2.1

Note. [a] As defined in Section 4.

in this object. We were unable to improve the light curve fits by lowering the target χ^2/N, as MEMECHO was unable to converge on a solution when we did so.

The best-fit velocity-delay maps for the other four objects, covering the full observed wavelength range for each, are shown in Figure 8. The parameters used in MEMECHO to create the velocity-delay maps are given in Table 2. We also show more detailed velocity-delay maps for each individual emission line recovered for each object in Figures 9–12. To aid the eye in comparing ionization-stratified BLR structure between different emission lines in each object, we also provide false-color maps in Figure 13, with each color representing a different emission line as described in the captions. We also created simulated velocity-delay maps for a few different BLR kinematic models to compare qualitatively with our recovered velocity-delay maps. These simulated maps are shown in Figure 14, and represent different BLR models around a black hole with $M_{BH} = 1 \times 10^7 M_{\odot}$. We see features reminiscent of these simple models in our recovered velocity-delay maps.

5.1. Comments on Individual Objects

5.1.1. Mrk 335

The velocity-binned analysis of Mrk 335 shows a definite velocity-dependent lag signature (Figure 1), and we clearly see similar structures in the velocity-delay maps of both the He II and Hβ emission lines (Figure 9). We see a chevron-shaped pattern in the He II line, with a lack of prompt response in the center and shorter delays in the wings, which is consistent with the signatures expected from an inclined disk or a spherical shell (Figure 14). In the Hβ emission, we see an asymmetric profile, with longer lags toward the blue end of the emission, and shorter lags toward the red end. This is suggestive of inflowing gas, as demonstrated in our simple infall models given in Figure 14. This also matches the signature we found in our initial velocity-binned analysis. The He II emission is confined to smaller delays, as is expected from photoionization models of the BLR. Also consistent with disk structure is the response of He II along a much wider velocity range than that of Hβ.

5.1.2. Mrk 1501

Fewer kinematic details are apparent in the recovered maps for Mrk 1501 than for the other objects in our sample. This may be a consequence of the noisier continuum and emission-line light curves obtained for this target. Nonetheless, we can still gain useful insights into the Hβ and Hγ-emitting regions of the BLR in this object. As with Mrk 335, we see evidence in the velocity-delay maps for inflow, with longer lags in the blue and shorter lags toward the red end of the Hβ and Hγ emission lines. This signature is closest to that of the "extended BLR" infall model shown in Figure 14. While this velocity-delay map is probably too low-resolution for any detailed modeling, we

the "mean" continuum light curve are highly correlated, so, for example, having 10 consecutive points 1σ from the light curve model is likely a 1σ deviation, not a 10σ deviation. However, the velocity-delay maps do not change significantly if we use random individual DRW realizations of the light curve instead of the mean, indicating that the mean light curve can be used to produce accurate velocity-delay maps. While this solution is not ideal, it is currently the best method we have for dealing with gaps in the observed continuum light curves pending a major effort to integrate the two distinct software packages (JAVELIN and MEMECHO).

5. TWO-DIMENSIONAL VELOCITY-DELAY MAPS

We were able to recover velocity-delay maps with MEME-CHO for four out of the five galaxies observed. The best maps are for 3C 120 and Mrk 335, while the ones obtained for PG 2130+099 and Mrk 1501 are somewhat less well-defined. The light curves for Mrk 6, on the other hand, do not seem to be well-fit by a simple echo model, and we were therefore unable to obtain two-dimensional velocity-delay maps for this object. Figure 6 shows the best model fits we were able to obtain for Mrk 6. While there is some evidence for velocity-dependent structure in the one-dimensional delay maps shown, the models do not successfully fit any of the short-term variations seen
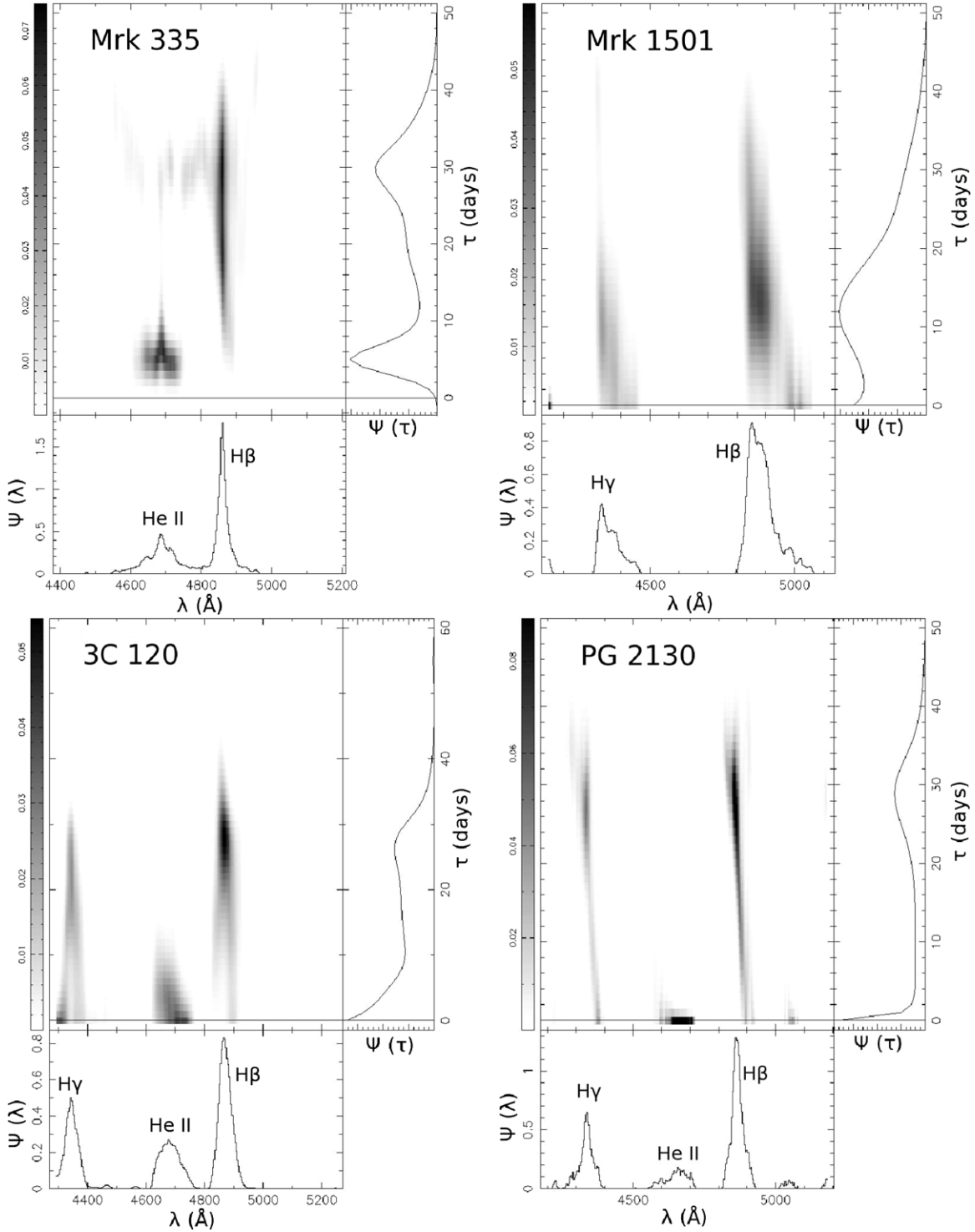
Figure 8. Our best-fit velocity-delay maps over the full rest-frame wavelength range for each object (gray scale), projections onto the rest-frame wavelength axis (bottom panel) and the time-delay axis (right panel). $\Psi(\lambda)$ is the overall response added up at each wavelength, and $\Psi(\tau)$ is the overall response of all emission lines added together at a given τ.

do see this same signature in our velocity-resolved analysis in Figure 1. There is also evidence for radial stratification of the BLR. Figure 13 shows there is a much stronger Hβ response at longer time lags than is observed for the Hγ emission. This is consistent with the idea that photoionization physics regulates the size of the BLR, as Hγ is a higher-energy transition and would therefore need to be located closer to the ionizing source than Hβ.

5.1.3. 3C 120

Our velocity-delay maps for 3C 120, shown in full in Figure 8, are the cleanest maps we were able to recover. We see evidence for radial stratification, with He II showing the shortest delays and Hγ and Hβ emitted at progressively larger radii. Figure 13 shows all three emission lines on one scale, with Hβ, Hγ, and He II shown in red, blue, and green, respectively, highlighting the
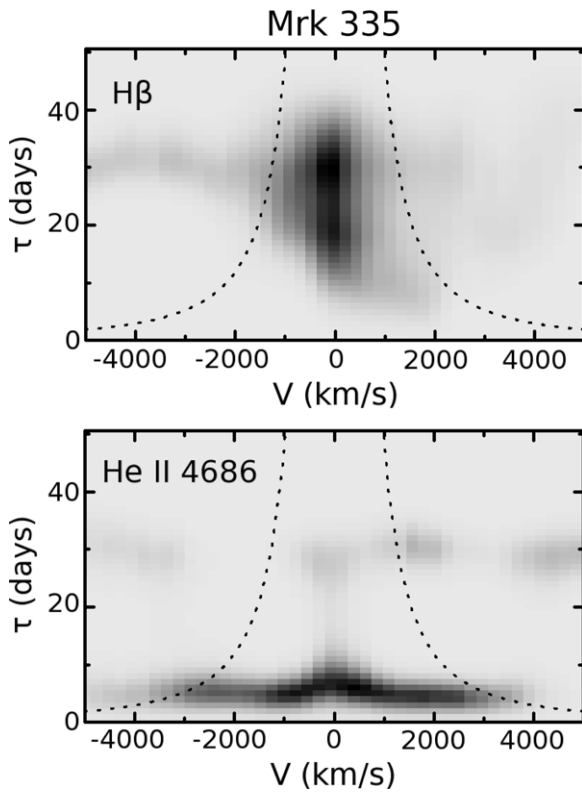
Mrk 335

Figure 9. Velocity-delay maps for both emission lines seen in Mrk 335. The dotted lines show the "virial envelope," $V^2\tau c/G = 4.6 \times 10^6 \, M_\odot$, measured from the mean time lag (Grier et al. 2012).
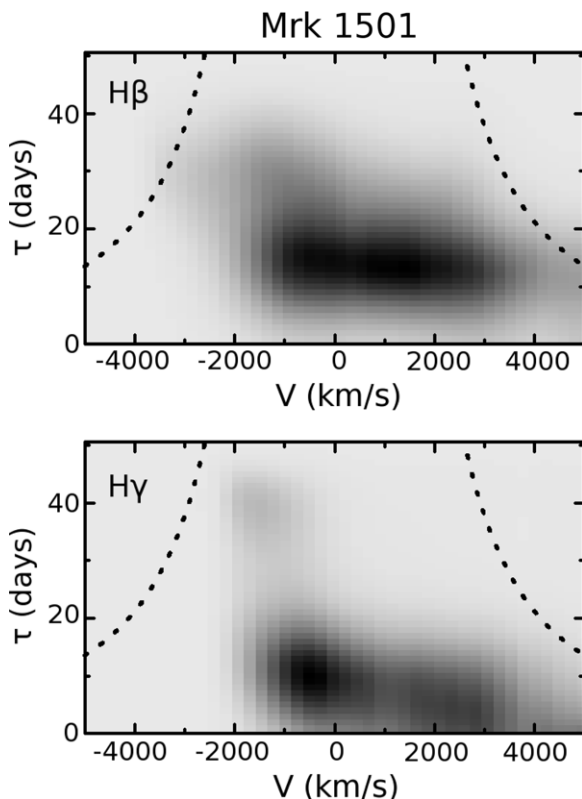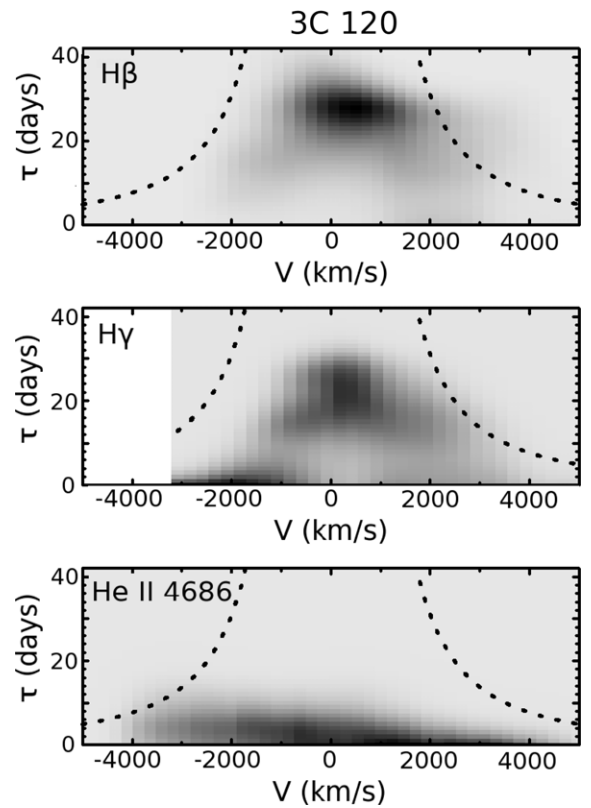
Mrk 1501

Figure 10. Velocity-delay maps for both emission lines seen in Mrk 1501. The dotted lines show the "virial envelope," $V^2\tau c/G = 3.3 \times 10^7 \, M_\odot$, measured from the mean time lag (Grier et al. 2012).

3C 120

Figure 11. Velocity-delay maps for all three emission lines seen in 3C 120. The dotted lines show the "virial envelope," $V^2\tau c/G = 1.2 \times 10^7 \, M_\odot$, measured from the mean time lag (Grier et al. 2012). The velocity-delay map for Hγ is truncated at $V \sim 3250 \, \mathrm{km \, s^{-1}}$ because the wavelength range of our spectrograph did not cover this far into the red.

radial stratification. The lack of a prompt response at line center in both Balmer lines indicates a deficit of material along the line of sight. The shape of the hydrogen response is consistent with signatures expected from an inclined disk or a spherical shell (Figure 14). This is similar to the signal found in NGC 5548 (Horne et al. 1991), Arp 151 (Bentz et al. 2010a), and Mrk 50 (Pancoast et al. 2012). We also see an asymmetry in the strength of the response in both the He II and Hβ emission profiles, nominally indicating inflow. The smaller velocity range of the Hβ and Hγ emission with respect to He II, combined with the radial stratification signatures, is consistent with disk structure.

5.1.4. PG 2130+099

The velocity-delay map for PG 2130+099 is somewhat noisier than that of 3C 120, and the model fits are not as good. However, the structure of the map is worth noting. While reverberation delays for the He II emission remain unresolved for this data, both the Hβ and Hγ emission lines clearly show velocity-resolved delay structure, with strong asymmetries as a function of velocity across the emission-line profile. This is similar to the Hβ emission we see in Mrk 335 and the He II emission in 3C 120. This asymmetry, with longer lags at the blue end of the emission line and shorter lags to the red, is suggestive of inflowing gas, and matches the "Infall (less-extended BLR)" model in Figure 14 quite well. In our analysis of the velocity-binned sections of the Hβ emission line (Figure 1), we see this same structure, so while the delay maps for this object are probably not good enough for any detailed modeling, they are consistent with the signatures of inflowing material already seen in this object.
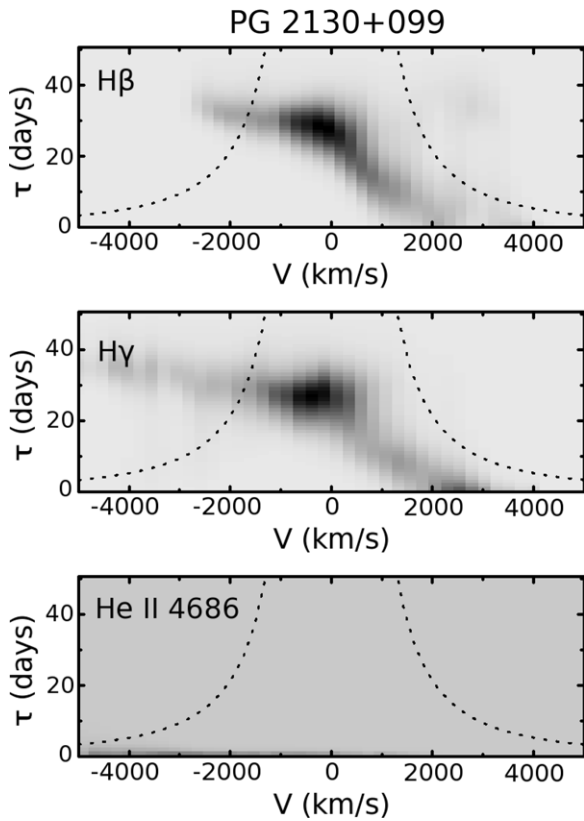
Figure 12. Velocity-delay maps for all three emission lines seen in PG 2130+099. The dotted lines show the "virial envelope," $V^2 \tau c/G = 8.3 \times 10^6 \, M_\odot$, measured from the mean time lag (Grier et al. 2012).

PG 2130+099 has long been a curiosity. Early on, Kaspi et al. (2000) measured a time lag of ~180 days in this object, placing it well above the $R_{BLR}-L$ relationship. Later studies by Grier et al. (2008) and Grier et al. (2012) found much shorter lags on the order of tens of days: Most recently, Grier et al. (2012) reported a mean Hβ time delay of $12.8^{+1,2}_{-0,9}$ days. These studies attributed the discrepancies to undersampled light curves combined with long-term secular changes in the Hβ equivalent width in the data from Kaspi et al. (2000). However, even with the new, shorter lag measurements, PG 2130+099 is still a major outlier from the $R_{BLR}-L$ relation, as it is now positioned far below the relation (Grier et al. 2012). Despite the higher sampling rate of the more recent campaigns, ambiguities remain as to whether the measured Hβ lags represent the true mean BLR radius, as the light curves were missing data at key points in time. We see in our velocity-delay map that the majority of the response in the Hβ emission seems to be centered on a delay of ~30 days (Figures 12 and 13).

To investigate this, we ran a one-dimensional delay map analysis of PG2130 +099 in MEMECHO to look for an indication of where the true lag lies. Figure 15 shows the model continuum light curve envelope in the bottom panel, and the Hβ light curve from Grier et al. (2012) in the top right panel; the top left panel shows the delay map recovered by MEMECHO. The MEMECHO model fits the data fairly well in this case, and there are two clear peaks in the delay map. The stronger peak is centered around 12.5 days, and the slightly weaker peak is centered at 31 days. We compare this with the two-dimensional velocity-delay map (Figures 8, 12, and 13), which shows a large signal on the blue side of the emission concentrated at around 30 days and a fainter signal to the redward side that stretches down to shorter lags. A plausible
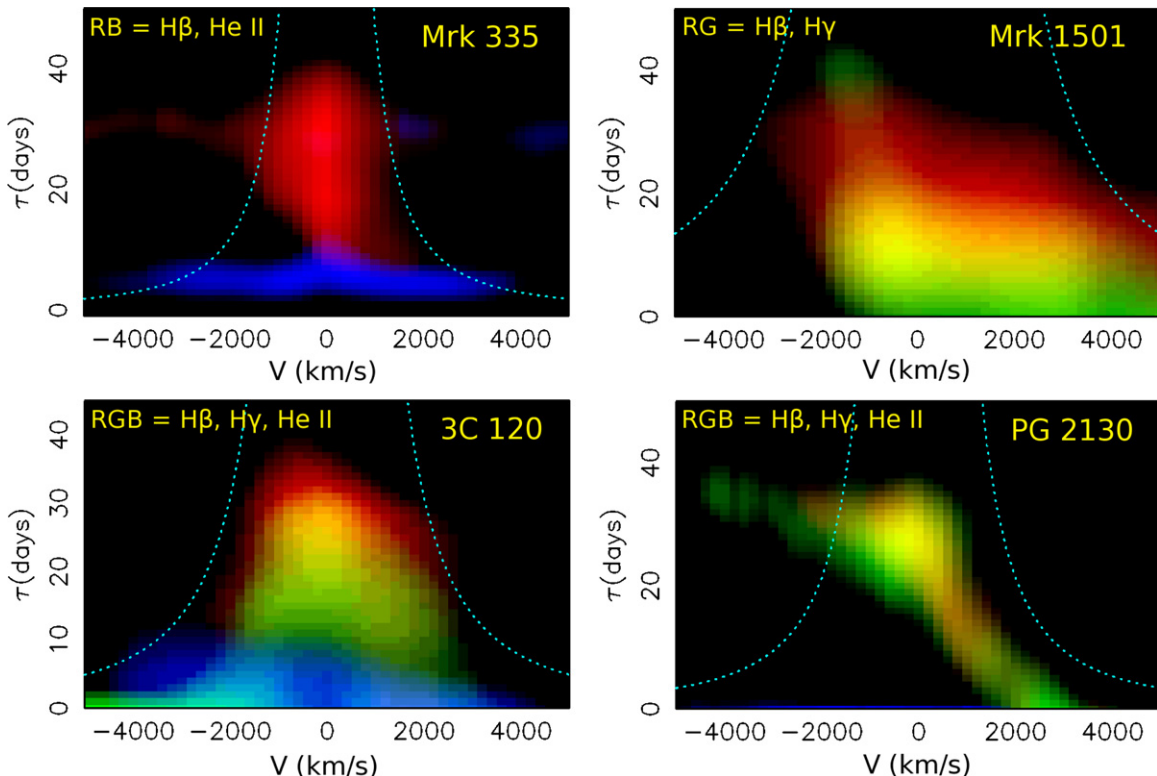

Figure 13. False-color velocity-delay maps for Mrk 335, Mrk 1501, 3C 120, and PG 2130+099. The dotted lines in each panel correspond to virial envelopes for each object as listed in Figures 9–12. The Hβ emission is shown in red, Hγ emission in green, and He II λ4686 emission in blue.

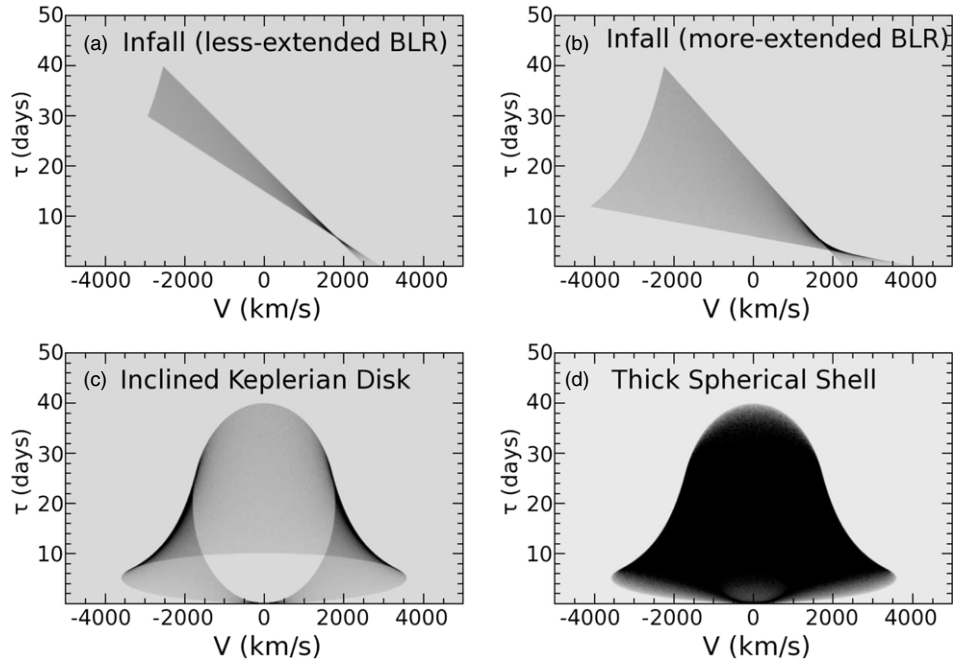(A color version of this figure is available in the online journal.)

Figure 14. Velocity-delay maps for simple BLR models of Hβ emission around a 1×10^7 $M_\odot$ black hole. Panel (a) shows highly beamed emission (typical for Hβ, see Ferland et al. 1992) from gas in free-fall motion. The infalling gas is distributed in a spherical shell with inner and outer radii of 15 and 20 light-days, inclined at an angle of 45 deg. Panel (b) shows the same infall model but with a more-extended BLR with inner and outer radii of 5 and 20 light-days, respectively. Panel (c) shows a map for an edge-on Keplerian disk with inner and outer radii of 5 and 20 light-days, and panel (d) shows a map for a fully illuminated thick spherical shell of Keplerian circular orbits, with inner and outer BLR radii of 5 and 20 light-days, respectively.
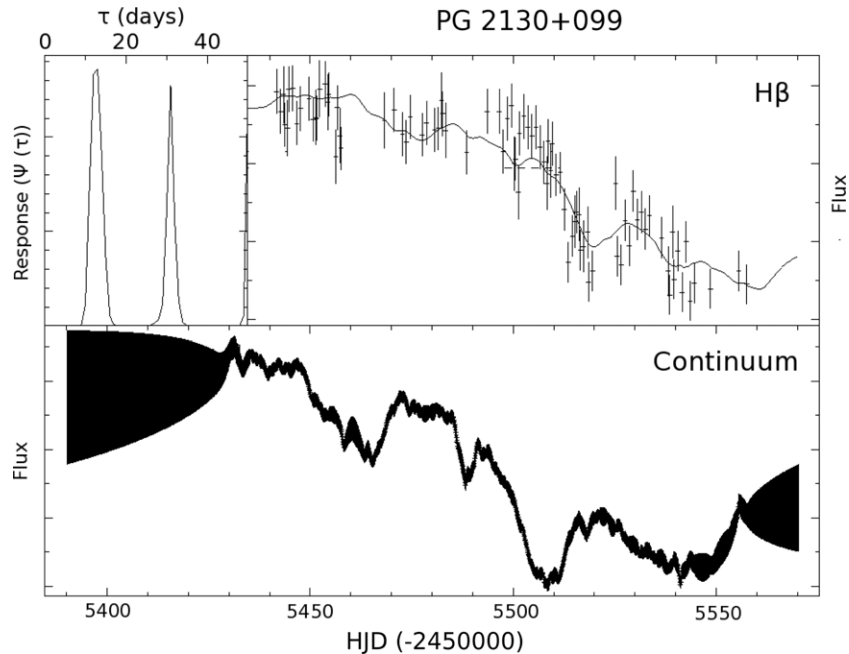
Figure 15. One-dimensional delay map for PG 2130+099. The bottom panel shows the simulated continuum light curve used in the MEMECHO analysis, with the errors shown as the black envelope. The top right panel shows the light curve for the entire Hβ emission line from Grier et al. (2012). The top left panel shows the one-dimensional delay map from MEMECHO.

model reproducing these results is a nearly face-on disk with the emitting gas located at around 30 light-days, combined with a strong inflowing gas component not necessarily within the plane of the disk. Including an inflow signature when we measure the flux of the entire Hβ emission line could cause our result to be skewed toward shorter mean lags, when the true distance of the virialized gas is closer to $\sim$30 days. Because of the lower quality and coarser sampling of the light curves for this object, we will likely be unable to model this structure in much more detail. However, it is clear from the delay map that the majority of the Hβ signal comes from a radius of $\sim$31 light-days. This radius puts PG2130+099 much closer to the $R_{\rm BLR}-L$ relation. This also increases the black hole mass estimate for PG 2130+099 by a factor of about 2.4, putting it at about 10^8 $M_\odot$.
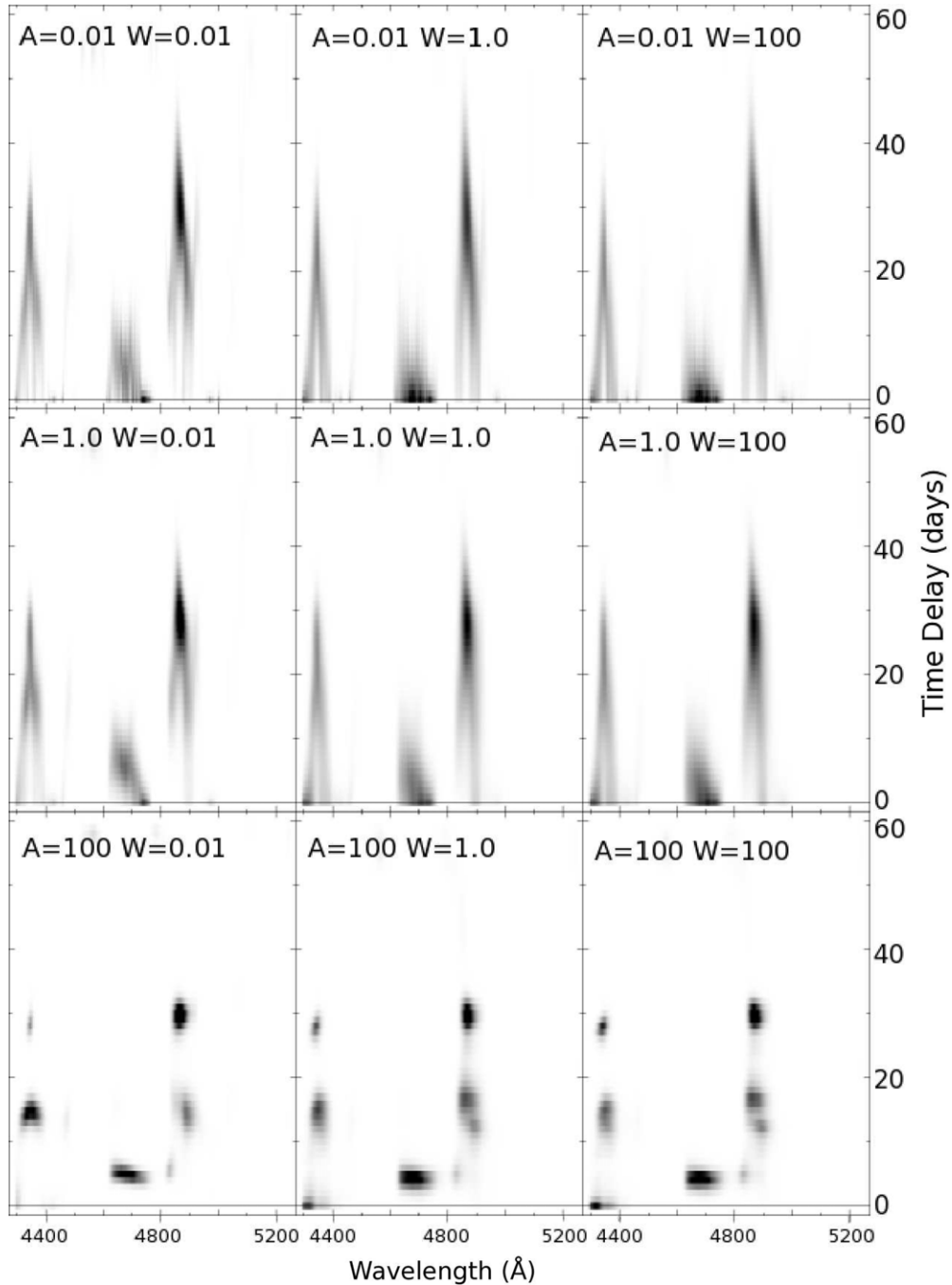
11

Figure 16. Velocity-delay maps for 3C 120. Each panel shows the best map found as we vary A and W by factors of 100. Increasing A smooths the maps more strongly in λ and less in τ, while increasing W reduces the importance of fitting the continuum model relative to the delay maps. All models are converged to the same overall goodness-of-fit χ^2/N. Our adopted velocity-delay map is that of the middle panel.

This would place PG 2130+099 definitely within the expected scatter of the M_{BH}–σ_* relation.

5.2. MEMECHO Parameters and Settings

5.2.1. The A and W Parameters

MEMECHO gives the user control over various aspects of the fitting process. We first consider the weights w_i (see Equation 4), which are implemented in MEMECHO as the user-controlled W and A parameters. The W parameter controls the weight given to pixels in $\Psi(\lambda, \tau)$ relative to the weight given to the pixels in the continuum model $C(t)$. Increasing W makes the delay map stiffer and allows for more flexibility in the continuum model.

A affects the aspect ratio of features in the velocity-delay map $\Psi(\lambda, \tau)$. The default values for $\Psi(\lambda, \tau)$ are geometric means of neighboring pixels, with A increasing the weight of neighbor pixels in the λ direction relative to those in the τ direction.

It is important that the structures we see in our delay maps are not dependent on our choices of A and W. To verify that our results are robust, we produced MEMECHO models altering the A and W parameters and changing the wavelength and velocity grids of the transfer function models. The panels of Figure 16 show the resulting velocity-delay maps for 3C 120 as we vary these parameters. For the most part, the general shape of our velocity-delay map is not affected by changes in A or W. However, if A is made too large, we start to over-fit the data and
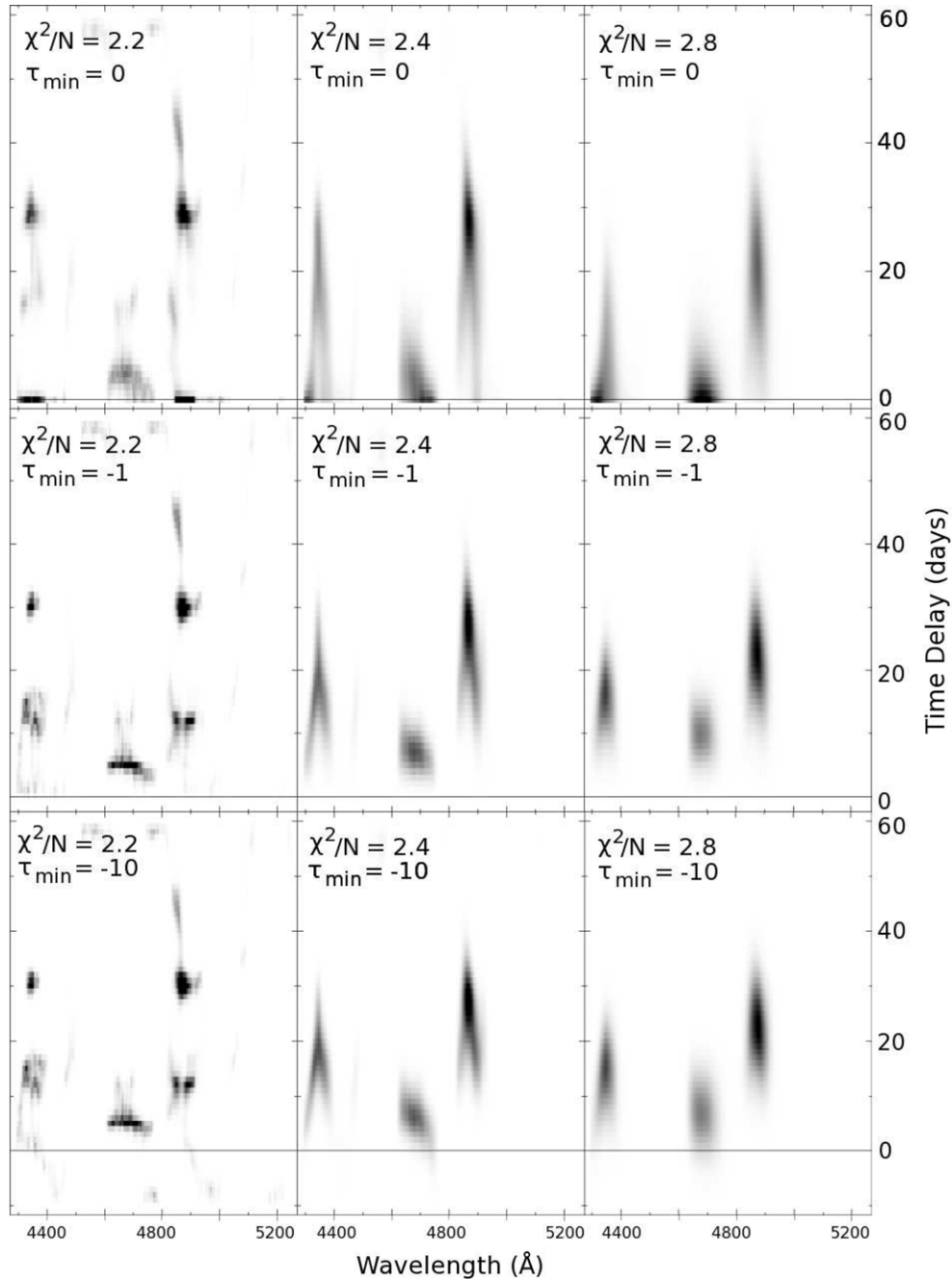
Figure 17. Velocity-delay maps for 3C 120, varying the degree of smoothing and the minimum lag allowed in the model (τ_{min}). Increasing values of χ^2/N mean that the entropy term is more heavily smoothing the map. Our adopted velocity-delay map is that of the top middle panel.

introduce spurious features into the maps. The stability with respect to the W parameter is expected, since the continuum light curve we are using is very highly sampled, and therefore very highly constrained. Since these behaviors are generic to all four objects, we only show the results for 3C 120.

5.2.2. The Minimum χ^2/N

We also investigated the effect of varying the target χ^2/N of the MEMECHO solution, as the final resolution of the recovered delay maps is controlled by this parameter. The choice of the target χ^2/N is a trade off between smoother, lower delay resolution maps for higher χ^2/N, and sharper but less reliable

structure in the maps at lower χ^2/N. Because we are using over-sampled continuum model light curves from JAVELIN, the actual value of χ^2/N is no longer strictly valid, because the continuum light curve data points are not fully independent. Therefore, our chosen values of χ^2/N reflect the best trade-off between delay-map resolution and reliable structure in the fits that we could obtain. Figure 17 shows velocity-delay maps for 3C 120 as we vary the χ^2/N, from left to right. As we lower the target χ^2/N, the structure eventually becomes more complex but also less reliable, as the fits are now producing structures to model the noise in the line light curves. However, the basic structure of the velocity-delay maps is robust to reasonable changes in the target χ^2/N.

13

5.2.3. Minimum Allowed Time Delays

When we vary the minimum lag τ_{min} that we allow MEME-CHO to consider, we also see a trend worth noting. Figure 17 shows that when τ_{min} is set to zero (top panels), the velocity-delay structure in the map also extends all the way to zero. However, when negative lags are allowed (middle and bottom panels), we see that the structure in the velocity-delay maps, particularly when considering the chevron-shaped structure in the Hβ and Hγ emission lines, peaks at a positive delay and is lower at $\tau = 0$ but does not extend to 0. This has to do with the way MEMECHO deals with its delay map models. The default is set to "pull" the response down to zero at the ends of the delay map when τ_{min} and τ_{max} are not equal to zero. Therefore, when $\tau_{min} = 0$, the default cannot pull down at the low-τ end, so the lowest-entropy map is an exponential function of τ. With $\tau_{min} < 0$, the entropy pulls down on both ends of the delay map, which then creates a Gaussian peak at positive delays.

Because of this, different values of τ_{min} can affect the final velocity-delay maps produced, as this effectively regulates the behavior of the model on some level when trying to smooth the delay maps to the default image. We currently have no means to evaluate which value of τ_{min} results in the "correct" velocity-delay map—it is therefore worth considering velocity-delay maps with various τ_{min} parameters, as we do here, when drawing conclusions about the BLR structure signatures, and any detailed modeling and interpretations should consider and evaluate the differences in these maps. In this work, we make only qualitative statements regarding the signatures seen in the velocity-delay maps. Whether or not the response actually reaches zero at any point in the 3C 120 maps is unknown, but for our purposes it is reassuring that all of the maps show the same basic structures and kinematic signatures. From Figure 17, comparing results for $\tau_{min} = -10, -1$, and 0, we can also evaluate the evidence for a deficit of prompt response from the resulting delay maps created with each value of τ_{min}. At all three values of τ_{min}, we see Gaussian delay distributions at positive lags in the core of Hβ and Hγ in 3C 120, but not for He II—thus the data provide evidence for a deficit of prompt response in the center of Hβ and Hγ, but not for He II. This behavior is consistent with our expectations for the stratification of the BLR.

6. SUMMARY AND CONCLUSIONS

We have presented velocity-delay maps constructed from the line and continuum variations observed in four objects from our 2010 reverberation campaign. These maps provide new insights into the structure of the BLR and constitute a dramatic increase in the number of objects that have at least some information on the velocity field of the BLR. Along with the velocity-delay maps for Arp 151 (Bentz et al. 2010a) and the models of Mrk 50 (Pancoast et al. 2012), these velocity-delay maps provide the strongest constraints on the structure of the BLR. Our velocity-delay map for 3C 120 shows very similar structure to the map of Arp 151, which also shows a lack of prompt response in the Balmer lines. The continuum light curves for Arp 151 were well-enough sampled that Bentz et al. (2010a) were able to recover a velocity-delay map using the original continuum light curve instead of substituting in simulated ones. The similarities between the maps for Arp 151 and our maps lends weight to the reliability of our results using the simulated continuum light curves. We also see very asymmetric profiles in both the Balmer and high-ionization emission that is suggestive of infalling gas in all of our objects. In 3C 120 and

Mrk 335, the transfer function structure for the Balmer lines differs from that for the He II λ4686 emission line, suggesting different structures dominating at different BLR radii. In all cases where our data are of sufficient quality to constrain the structure of the BLR, we see clear evidence of infall and rotation, both of which result from the gravitational influence of the black hole. As gravitationally dominated motion is the key assumption of reverberation mapping, our results strongly support the reliability of black hole mass estimates derived from reverberation mapping. Detailed modeling of our most well-defined velocity-delay maps and a complete discussion of the implications will follow in a future work.

REFERENCES

Antokhin, I. I., & Bochkarev, N. G. 1983, AZh, 60, 448
Bahcall, J. N., Kozlovsky, B.-Z., & Salpeter, E. E. 1972, ApJ, 171, 467
Bentz, M. C., Horne, K., Barth, A. J., et al. 2010a, ApJL, 720, 46
Bentz, M. C., Walsh, J. L., Barth, A. J., et al. 2010b, ApJ, 716, 993
Blandford, R. D., & McKee, C. F. 1982, ApJ, 255, 419
Bochkarev, N. G., & Antokhin, I. I. 1982, ATsir, 1238, 1
Capriotti, E. R., Foltz, C. B., & Peterson, B. M. 1982, ApJ, 261, 35
Clavel, J. 1991, in Variability of Active Galaxies, ed. C. M. Duschl, S. J. Wagner, & M. Camenzind (Berlin: Springer), 31
Clavel, J., Boksenberg, A., Bromage, G. E., et al. 1990, MNRAS, 246, 668
Clavel, J., Reichert, G. A., Alloin, D., et al. 1991, ApJ, 366, 64
Clavel, J., Wamsteker, W., & Glass, I. S. 1989, ApJ, 337, 236
Crenshaw, D. M., & Blackwell, J. H., Jr. 1990, ApJL, 358, 37
Denney, K., Assef, R. J., Benz, M., et al. 2011, in Narrow-Line Seyfert 1 Galaxies and their Place in the Universe, ed. L. Foschini et al. (Trieste: Proc. of Sci.), 34
Denney, K. D., Peterson, B. M., Pogge, R. W., et al. 2009, ApJL, 704, 80
Denney, K. D., Peterson, B. M., Pogge, R. W., et al. 2010, ApJ, 721, 715
Dietrich, M., Kollatschny, W., Peterson, B. M., et al. 1993, ApJ, 408, 416
Doroshenko, V. T., Sergeev, S. G., Klimanov, S. A., Pronik, V. I., & Efimov, Y. S. 2012, MNRAS, 426, 416
Ferland, G. J., Peterson, B. M., Horne, K., Welsh, W. F., & Nahar, S. N. 1992, ApJ, 387, 95
Gaskell, C. M. 1988, ApJ, 325, 114
Grier, C. J., Peterson, B. M., Bentz, M. C., et al. 2008, ApJ, 688, 837
Grier, C. J., Peterson, B. M., Pogge, R. W., et al. 2012, ApJ, 755, 60
Guerras, E., Mediavilla, E., Jimenez-Vicente, J., et al. 2012, arXiv:1207:2042
Horne, K. 1994, in ASP Conf. Ser. 69, Reverberation Mapping of the Broad-Line Region in Active Galactic Nuclei, ed. P. M. Gondhalekar, K. Horne, & B. M. Peterson (San Francisco, CA: ASP), 23
Horne, K., Peterson, B. M., Collier, S. J., & Netzer, H. 2004, PASP, 116, 465

Horne, K., Welsh, W. F., & Peterson, B. M. 1991, ApJL, 367, 5
Kaspi, S., Smith, P. S., Netzer, H., et al. 2000, ApJ, 533, 631
Kelly, B. C., Bechtold, J., & Siemiginowska, A. 2009, ApJ, 698, 895
Kollatschny, W. 2003, A&A, 407, 461
Kollatschny, W., & Dietrich, M. 1997, A&A, 323, 5
Koratkar, A. P., & Gaskell, C. M. 1989, ApJ, 345, 637
Kozłowski, S., Kochanek, C. S., Udalski, A., et al. 2010, ApJ, 708, 927
Krolik, J. H., Horne, K., Kallman, T. R., et al. 1991, ApJ, 371, 541
MacLeod, C. L., Ivezić, Ž., Kochanek, C. S., et al. 2010, ApJ, 721, 1014
MacLeod, C. L., Ivezić, Ž., Sesar, B., et al. 2012, ApJ, 753, 106
Pancoast, A., Brewer, B. J., & Treu, T. 2011, ApJ, 730, 139

Pancoast, A., Brewer, B. J., Treu, T., et al. 2012, ApJ, 754, 49
Peterson, B. M. 1993, PASP, 105, 247
Peterson, B. M., Balonek, T. J., Barker, E. S., et al. 1991, ApJ, 368, 119
Peterson, B. M., Ferrarese, L., Gilbert, K. M., et al. 2004, ApJ, 613, 682
Sergeev, S. G., Doroshenko, V. T., Dzyuba, S. A., et al. 2007, ApJ, 668, 708
Ulrich, M.-H., & Horne, K. 1996, MNRAS, 283, 748
van Groningen, E., & Wanders, I. 1992, PASP, 104, 700
Wanders, I., Goad, M. R., Korista, K. T., et al. 1995, ApJL, 453, 87
Wanders, I., & Peterson, B. M. 1996, ApJ, 466, 174
Zu, Y., Kochanek, C. S., Kozłowski, S., & Udalski, A. 2012, arXiv:1207.3794
Zu, Y., Kochanek, C. S., & Peterson, B. M. 2011, ApJ, 735, 80